Line Identification and Temperature Diagnostics of Eta Carina's Sr-Filament

Henrik Rhodin

Lund Observatory
Lund University

Line Identification and Temperature Diagnostics of Eta Carina's Sr-Filament

Henrik Rhodin

Supervisor: Henrik Hartman

Lund Observatory

February 20, 2013

Abstract

This bachelor thesis concerns the NIR spectral region of the Sr-filament, a substructure of the fan located in the equatorial skirt of Eta Carinae. The primary objective was to identify emission features intrinsic to the Sr-filament, and to tabulate these in a line-list spanning the spectral range $\lambda\lambda 990 - 2410\ nm$. A secondary objective was concerned with the use of identified parity-forbidden atomic transitions for temperature diagnostics. The thesis is based on a long-slit NIR spectrum at resolution $R \backsim 10500$, obtained using the ESO X-Shooter instrument at VLT. Centred on the Sr-filament, at a position offset 2.0 arcsec NW of the central object, the target is sampled during the recovery phase of Eta Carinae's spectroscopic cycle. 300 emission features spectrally separated the Sr-filament from other sub-structures. Out of these, 144 lines were identified. One Zr II line and two Co II lines are identified, but not confirmed by previous studies. The resulting line-list indicates that the NIR spectrum of the Sr-filament is dominated by CaI, TiII and FeI emission, accounting for $\backsim 75\%$ of the identified features. [TiII] lines are proposed as candidates for temperature diagnostics due to a span in excitation energy and wavelength. However, a lack of reference atomic transition probabilities prevented numerical calculations being conducted.

Populärvetenskaplig Sammanfattning

Eta Carinae är en av Vintergatans största och ljusstarkaste stjärnor, och strålar ut lika mycket ljus på 6 sekunder som solen strålar ut på ett helt år. Stjärnstoft, gas och småpartiklar som samlats i stora moln tyder på att Eta Carinae har genomgått stora utbrott, som sedermera gett upphov till formen på stjärnan och dess omgivning. Idag befinner sig Eta Carinae i ett stabilt tillstånd, som avbryts av regelbundna perioder med minde utbrott under vilka stjärnan ändrar mängd (magnitud) och energifördelning (spektrum) av det utskickade ljuset. Eftersom systemet ligger i vår egen galax, så ligger det närmare oss än vad många andra stjärnor gör. Därför kan man titta på systemet i mer detalj än vad som är möjligt för andra stjärnor längre bort. Detta gör att man har kunnat identifiera småskaliga strukturer i det kringliggande gasmolnen.

En sådan struktur, med många starkt avvikande egenskaper har identifierats 2 bågsekunder från stjärnan. Denna struktur heter *Strontium Filamentet* (Sr-Filamentet) på grund av att man identifierat ovanliga linjer från en gång joniserat strontium. I detta kandidatarbete tittar man närmare på ett nära-infrarött (NIR) spektrum av Sr-Filamentet, och försöker att identifiera linjer som kan kopplas till olika atomövergångar i olika grundämnen och joner. Man hoppas att detta i sin tur kommer hjälpa oss att förstå hur Sr-Filamentet fungerar, vad det har för egenskaper, hur det påverkas av stjärnans strålning och i fall Sr-Filamentet spelgar processer som händer i stjärnan själv. Resultaten tyder på att det finns mycket linjer från neutralt järn, neutralt kalcium och en gång joniserat titan. Vissa av linjerna som observerats är sällysnt förekommande, men ses på grund av just de omständigheter som råder i Sr-filamentet. Dessa övergångar har egenskaper som gör dem bra för bestämning av olika fysikaliska parametrar så som temperatur. Sådanna övergångar från en gång joniserat titan föreslås som lämplig kandidat för vidare temperatur diagnostik.

Contents

1 Introduction

Eta Carinae is a massive stellar system with a central object ($\eta\,Car$), a bipolar Homunculus nebulae, and an equatorial skirt crossing the midplane, perpendicular to the polar axis. A dense stellar wind, processed nebulae ejecta and a spectroscopic cycle of $\smile$ 5.5 years contribute to the extreme spatial, temporal and spectral complexity that characterises the system. A dense region residing within the equatorial skirt at 2 arcsec NW of the central object, the *StrontiumFilament* (Sr-filament), shows blueshifted emission moving at a characteristic velocity of $\smile$ 100 kms^{-1} as well as strange emission lines of [Sr II] not observed in any other region of the Homunculus or other astronomical object Hartman et al. (2004).

In the words of Paul W. Merrill, *"Astronomical observations may thus supplement those of the laboratory by supplying data on line emission under very low densities. The character and intensity of the incident radiation may also play an important part in the duration of various electronic states. The problem can, of course, be worked both ways, and forbidden lines may thus perhaps yield information concerning conditions in the stars"* - Februrary 1928

In this spirit, the Sr-filament and the surrounding spray of nebulae ejecta may reflect radiation mechanisms and dynamic behaviour of the central object. Therefore, knowledge of the conditions, and of the behaviour of the external regions of the system may aid our understanding and give insights to the nature of the central object itself. Its characteristic features, in combination with its proximity and brightness allows detailed multiwavelength study to test astrophysical theories of stellar structure, stability and evolution. The infrared (IR) spectrum provides a unique diagnostic tool of the wind and the ejecta by mitigating the blend of narrow intrinsic emission lines of external structures with reflected stellar emission observed in the visual spectral range. Furthermore, the low excitation in the IR allows probing of the inner Homunculus regions to study embedded structures and their kinematics, Smith (2002).

This thesis intends to investigate a NIR spectrum of the Sr-filament, spanning the wavelength region of $\lambda\lambda 990 - 2410\ nm$, with a primary goal of constructing a line-list. A secondary focus consists of identifying parity-forbidden atomic transitions, from the constructed line-list, that could be used for a temperature parameter diagnostic tool. The overarching aim of the work is conveyed in operational questions, that intend to provide a set of goals and objectives to strategically guide the research throughout the analysis. These include; *How are intrinsic emission lines, characteristic of the Sr-filament identified and distinguished from those of other nebulosity structures? What are the physical conditions within the Sr-filament, and how are these influenced by the incident radiation? What can the emergent radiation tell us about the incident radiation? - and in extension, of the stellar object itself? Does an obtained temperature reflect the assumptions of the analysis? Are the results consistent with previous studies?*

In broad terms, the thesis consists of three sections. The theory section presents important results of previous work relevant to the thesis, as well as the physical framework in which the thesis is set. The experiment section defines the data acquisition and procedure, followed by a section on the obtained result and the associated analysis. The work is primarily based on Xshooter data obtained with VLT Xshooter, (P.I. Jose Groh), and on the results of the paper by

Hartman et al. (2004). It uses atomic reference data from NIST Database, Kurucz Database and *Multiplet Tables of Astrophysical Interest*, Moore (1945a) & Moore (1945b). The thesis is conducted as a third year bachelor student project at Lund University. I acknowledge that I am writing without full knowledge of Eta Carinae, the Sr-filament, nor of all astrophysical diagnostic tools for temperature and density determination. The results and the associated analysis is limited by my knowledge on the matter, and reflects the assumptions of the developed framework.

2 Theory

2.1 Object of Study

2.1.1 Eta Carinae

Eta Carinae (η Car) is a stellar system with a *Luminous Blue Variable* (LBV) central star, with a luminosity of $5 \cdot 10^6$ $L_\odot$ and a characteristic temperature of 25000K, Hartman et al. (2004). The system portrays two extended bipolar lobes around the inner core, hypothesised to be several solar masses of material ejected as shockwaves in two consecutive outbursts. The ejected material constitute defined shell-structures with characteristic properties, manifested in the expanding *Homunculus*, and the *Little Homunculus*. The Homunculus is primarily composed of neutral gas, with molecular Hydrogen in its cool exterior, whilst spectral analysis of the Little Homunculus reveal an internal emission nebulosity, Smith (2002).

Observations of dust-scattered radiation from η Car indicates the presence of an *equatorial skirt* in the plane intersecting the bipolar lobes of the Homunculus. Extending a few arcsec Northwest of the central object, a prominent structure associated with the equatorial spray is defined as the *Fan*. Studies suggest that the Fan traces the dust column-density minimum in the equatorial ejecta. This results in absence of intrinsic emission in the Fan, which therefore appears as a hole through which the Northwest polar lobe can be probed, Smith (2002). As it is associated with minimal nebulae ejecta, the Fan acts as a mechanism, extending the photon mean free path, allowing UV radiation from the central stellar source to escape to larger radii and excite equatorial gas. This explains apparent Fe II, Cr II etc. near ultraviolet emission lines that contribute to the *purple haze* within the Northwest lobe of the Little Homunculus, observed in line of sight of the Fan, Smith et al. (2004).

In the vicinity of the Homunculus midplane, bright emission and reflection objects B, C and D are localized in an 0.3" region, within a radius of 0.4" Northwest of the central source. The objects constitute Weigelt blobs; dense ($n_e \sim 10^7 - 10^8$ cm^{-3}), warm ($T_e \sim 6000 - 7000$ K) and slow moving (~ 40 kms^{-1}) condensations dominated by neutral (H^0) gas and heavily carbon-nitrogen-oxygen (CNO) -processed nebula material that has undergone fusion reactions in the core prior to ejection from the central source. The Weigelt blobs radiate strong narrow intrinsic emission lines in addition to reflecting the star's light, suggesting that they are *diffuse nebulae regions*. Little is known about the fainter emission/reflection regions, in between the blobs, but altogether the ensemble of nebular material, dominated by the bright Weigelt blobs is defined as the *inner ejecta* of Eta Carinae, Hamann (2012).
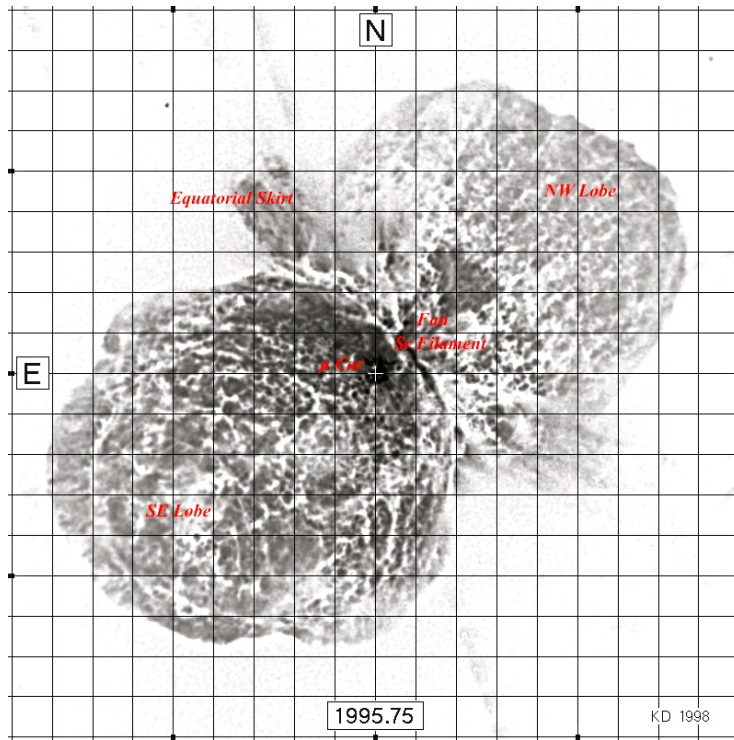
Figure 1: A HST/WFPC2 camera image of η Carinae imaged from observations in late 1995. An astrometric grid with grid spacing 1 arcsec has been superimposed for coordinate orientation J2000. Imaged in grayscale, the figure depicts morphology and structural components of the system. The photo is centred on the stellar primary, defined by the cross "+". A filter in the red wavelength band was used to image red continuum light reflected by dust and nebular scattering. The image has been edited by the author, and relevant structures are identified and labeled accordingly. Image prior to being edited is taken from Davidson (1999).

A 5.52-year period in the high excitation nebular and stellar emission lines of η Car has been identified. Variations between the spectroscopic minimum in 1998 and the broad maximum during the 1999 and 2000 demonstrate that lines of higher excitation disappear during the spectroscopic minimum only to reappear as the system recovers, including various H Lyα-pumped Fe II lines, Hamann (2012). The regularity of the 5.52-year cycle is interpreted as evidence that the central object is a binary of corresponding period, where the binary companion is hotter than the primary, but less luminous. Assuming a highly eccentric orbit allows interactions to occur for a brief time at close range, during which the hot companion plunges deep inside the dense primary wind. This would result in an obscuration of its contribution to the emergent far-UV emission before recovering, only to contribute to the ionisation and excitation of the inner ejecta at large separations. The matter is not resolved, however the modelled binary is a strong candidate due to its explanatory power of the characteristic intensity variation of emission features throughout the spectroscopic cycle, Hamann (2012).

2.1.2 The Strontium Filament

In a region of the fan, located 1.5 - 2" Northwest of η Car, faint, narrow and blueshifted emission lines have been identified in a 1" emission filament of nebulosity. The identified spectral lines have similar spatial and velocity structure, indicating that they originate from the same volume moving at a characteristic speed of $-100 \ kms^{-1}$. However, unusual excitation, low-ionization features and strange kinematics, as well as the identification of [SrII] emission lines not previously observed in other emission nebulae led to the identification of a new sub-structure, the Sr-filament, in the nebulosity of η Car, Hartman et al. (2004). The two resonance lines of Sr II at $\lambda 4078$Å and $\lambda 4216$Å were observed in emission, Hartman et al. (2004), and line ratios are consistent with electron densities of $10^7 \ cm^{-3}$ in a predominantly neutral region, Bautista et al. (2002).

Hartman et al. suggest that the strontium filament occupies the same spatial extent as the purple haze seen in HST images of η Carinae by Smith et al. (2004), with a two-component velocity spread along the equatorial plane forming a single closed structure, a ring/loop in velocity space, Hartman et al. (2004). Projected along the line of sight of the Sr-filament, emission-line features from various structures are observed. Prior studies, Smith (2002), suggest that such structures include the equatorial skirt, the receding northwest polar lobe of the Homunculus and the Little Homunculus. The structures can be differentiated by Doppler shift considerations, as each structure has a characteristic velocity.

Studies have shown that the spectrum of the Sr-filament is essentially a lower-ionisation version of Weigelt blob spectra, dominated by emission from species such as CI, MgI, CaI, CaII, ScII, TiII, VII and MnII in addition to signature SrII lines, Hartman et al. (2004) & Hamann (2012). Analysis of the Weigelt blobs suggests that the dominant underlying mechanism causing the Sr-filament, along with most of the inner ejecta, to be emission regions is radiative flux from the central object. However, Hamann (2012) argues that the strong metal line emissions from both the blobs and the Sr-filament are excited by a combination of collisions and photo-absorption of the stellar visible and near-UV flux, i.e. by continuum pumping. Most of the excitation of the Sr-filament appears to be due to mid-UV and near-UV radiation, observed to have low variability across the minimum of the spectroscopic cycle. Smith (2002) conducted an investigation, using the purple haze as a tracer of spectroscopic variability in the Sr-filament across the 5.5 year cycle. No significant variability associated with the Sr-filament was observed, Hartman et al. (2004).

2.2 Quantum Mechanical Selection Rules and Metastable States

A quantum mechanical treatment of atomic systems, assuming a Coulomb potential and a transformation of the Laplacian operator ∇^2 to spherical coordinates generates a separable solution to the Hamiltonian of the form $\Psi(r, \theta, \phi) = R(r)Y(\theta, \phi)$ where $R(r)$ defines the radial wavefunction and $Y(\theta, \phi)$ defines the angular wavefunction. The physical interpretation of the wavefunction Ψ as a probability amplitude requires that the eigenfunctions of Ψ satisfy the following mathematical conditions: they must be single-valued, continuous and possible to normalize. The conditions, applied on the solution, generate a set of quantum numbers n, l, and m that define the eigenfunctions of each possible eigenstate

of a one-electron atomic system. Using the quantum numbers, the solution of the Hamiltonian can be written as,

$$\psi_{nlm}(r,\theta,\phi) = R_{nl}(r)Y_{lm}(\theta,\phi) \tag{1}$$

where $R_{nl}(r)$ represents the solutions to the radial function, and $Y_{lm}(\theta,\phi)$ defines the spherical harmonics. An important property of the wavefunctions is that when the parity operator $\mathcal{P}$ acts on an arbitrary function $f(\overline{r})$ it causes an inversion of the position coordinate $\overline{r}$ through the origin such that $\mathcal{P} \cdot f(\overline{r}) = f(-\overline{r})$. It follows that if $\mathcal{P} \cdot \psi(\overline{r}) = \psi(\overline{r})$, i.e. $\psi(-\overline{r}) = \psi(\overline{r})$, then the wavefunction ψ is defined to be even. In contrast, $\psi(-\overline{r}) = -\psi(\overline{r})$ is defined to be odd. The parity operator in polar coordinates generates transformations of the form $r \to r, \theta \to (\pi-\theta), \phi \to (\pi+\phi)$. Whilst the radial wavefunction is unaffected by the parity operator, the spherical harmonics are subject to transformations of the form $Y_{lm}(\theta,\phi) \to (-1)^l Y_{lm}(\theta,\phi)$. It follows that the parity of a wavefunction is determined by the quantum number l such that parity π can be expressed as $\pi = (-1)^l$: the wavefunction is *odd* when l is odd, and *even* when l is even.

Generalised many-electron atomic systems, the solution to the Hamiltonian can be expressed as a linear combination of one-electron radial wavefunctions and a spherically symmetric potential. As each wavefunction has the same angular dependence as the hydrogenic wavefunctions, it follows that the parity of a configuration is given by the parity of $\sum_i l_i$.

Excited atomic states decay radiatively by emission of a photon, assuming the absence of a perturbing field or particle. The *radiative lifetime* is defined as the expected time that the atom resides in an excited state, followed by a radiative decay. The magnitude of the radiative lifetime is determined by the sum of individual rates of the decay channels resulting in energetically lower states. The radiative lifetime, τ_i, for a state i is defined as

$$\tau_i = \frac{1}{\sum_k A_{ik}} \tag{2}$$

where A_{ik} is the transition probability for the transition from level i to level k. It is important to note that different decay channels from a given upper level are not equally probable. A level combines strongly or weakly with different lower states i.e. have a high/low transition probability respectively.

The transition probability is an important atomic parameter in plasma diagnostics of spectral lines. A quantum mechanical treatment expresses the atomic transition probability as proportional to the matrix element $| < \psi_f|O|\psi_i > |^2$, where the operator $O = e\overline{r}$ defines the radiation field connecting the initial with the final atomic state, Thorne et al. (2007). Electric dipole radiation (E1) is the dominating type of radiation, connecting atomic states of opposite parity by *allowed transitions* with transition probabilities of the order $A \sim 10^8 s^{-1}$. The dipole operator is a one-electron operator, and involving only *one* electron changing its state. For the dipole interaction $| < \psi_f|e\overline{r}|\psi_i > | = e \int \Psi_f^* \overline{r} \Psi_i d\overline{r}$ the radial parameter $\overline{r}$ changes sign by inversion at the origin. It follows that in a many-electron system, all the contributions from all values of r to the integral will cancel, unless the product $\Psi_f^* \Psi_i$ also changes sign i.e. the product of the two wavefunctions has odd parity. It follows that the initial and final states must have opposite parities. As the parity varies as $\pi = (-1)^l$, it follows that the l of the electron making the transition must change by 1, 3, ... Mathematical treatment of the angular part of the wavefunctions shows that only a

change of *one* unit is allowed, giving the selection rule $\Delta l = \pm 1$. Similarly, the J quantum number measuring the total angular momentum is well defined for any atomic system, obeying the selection rule $\Delta J = 0, \pm 1$ with the constraint $J = 0 \rightarrow J = 0$ not allowed. The above constitute *rigorous selection rules*, independent of the coupling scheme defining a specific atomic structure, and are summarised in Table 1.

Even-parity metastable levels cannot decay/be connected by E1 transitions, as these require a parity change. Under these conditions, electric and magnetic multipole radiation is possible, and besides E1, magnetic dipole (M1) and electric quadrupole (E2) transitions have the highest probability. Operators of M1 and E2 transitions do not include a parity change, and thus, transitions connecting states of the same parity allows decay channels for metastable states. In the context of *astrophysics*, these transitions generate *forbidden lines*. The transition probability for M1 and E2 transitions are of the order $A \sim 1s^{-1}$. It follows that if an excited level can decay by an E1 transition, the M1 and E2 emission will be negligible. But if no E1 decay channels are available, the forbidden M1 and E2 lines dominate.

Apart from the rigorous selection rules, a second set of selection rules associated with the conditions/assumptions specific to the coupling scheme used can be formulated. To exemplify this, the LS coupling scheme places constrains on the total orbital and total spin angular momenta, L and S. LS coupling is often a good approximation for the lightest elements and for low configurations, and selection rules may therefore be valid for forbidden transitions in astrophysical plasmas or nebulae that to a large extent constitute of light elements. However, in general, different parts of the total energy level system in complex spectra are represented by different coupling schemes. The properties of E1, M1 and E2 transitions are summarized in Table 1.

Table 1: Quantum Mechanical Selection Rules

E1	M1	E2
	Rigorous Selection Rules	
Parity Change	No Parity Change	No Parity Change
$\Delta J = 0, \pm 1$	$\Delta J = 0, \pm 1$	$\Delta J = 0, \pm 1, \pm 2$
$(0 \nleftrightarrow 0)$	$(0 \nleftrightarrow 0)$	$(0 \nleftrightarrow 0, 1/2 \nleftrightarrow 1/2, 0 \nleftrightarrow 1)$
	LS Selection Rules	
$\Delta S = 0$	$\Delta S = 0$	$\Delta S = 0$
$\Delta L = 0, \pm 1$	$\Delta L = 0$	$\Delta L = 0, \pm 1, \pm 2$

In the following thesis the use of the LS notation is restricted to represent the atomic state or configuration and does not strictly convey the coupling scheme of the configuration. Forbidden lines are denoted/designated by the spectroscopic notation of the element inserted in square brackets, e.g. [Fe II] for forbidden Fe II lines.

2.3 Forbidden Lines as a Diagnostic Tool

In a plasma at Local Thermodynamic Equilibrium (LTE) conditions, the population equilibrium is created by collisions, so that the shortfall of radiative energy does not matter. Therefore, an excited state must have a higher probability of

de-excitation by collision than by spontaneous emission. In complete thermodynamic equilibrium, atomic states are populated according to a Boltzmann distribution, and the thermodynamic principle of detailed balance governs the energy balance of the system. The equality must hold separately for collisional and radiative processes and for all pairs of levels individually, mathematically expressed as

$$n_1 \rho B_{12} + n_1 n_e C_{12} = n_2 \rho B_{21} + n_2 A_{21} + n_2 n_e C_{21} \tag{3}$$

where n_1 and n_2 are the populations of two states, ρ is the radiation density at the frequency v_{12}, B_{12} is the absorption coefficient, n_e is the electron density, B_{21} is the stimulated emission coefficient, A_{21} is the spontaneous emission coefficient, and C_{12} and C_{21} are the collisional absorption and emission coefficients respectively. For low radiation density, ρ, the expression can be reformulated as

$$\frac{n_2}{n_1} = \frac{n_e C_{12}}{n_e C_{21} + A_{21}} \tag{4}$$

An upper level that can only decay through parity-forbidden transitions is defined to be a metastable state, with a radiative lifetime of the order of seconds, compared to ordinary excited states with lifetimes in the nanosecond regime. Under the conditions of dilute astrophysical plasmas, such as nebular regions characterised by large volumes and low particle density, the probability for collisional deexcitation is negligible, and metastable states undergo radiative decay by forbidden transitions. The specific properties of forbidden lines tend to make them useful as a diagnostic tool in the analysis of nebulae and other thin astrophysical plasmas. The reason being that measurements of intensity ratios of certain pairs of lines can give a good estimate of physical parameters such as temperature and density without detailed modelling or knowledge of parameters such as geometry and ion abundance, Osterbrock & Ferland (2006).

For metastable states, an equilibrium is reached when the number of collisional excitations to the state per unit time is equal to the number of emitted photons; *coronal equilibrium*. Imposing nebulae conditions assuming a negligible radiation density, and a low electron density such that $A_{21} \gg n_e C_{21}$, and dictating that excitations are due to electron collisions whilst deexcitations occur by spontaneous emission, the principle of detailed balance condenses to

$$\frac{n_2}{n_1} = \frac{n_e C_{12}}{A_{21}} \tag{5}$$

The equation states that the electron density and the two rate coefficients must be known to determine the population ratio. Furthermore, the imposed condition $A_{21} \gg n_e C_{21}$ results in a population ratio n_2/n_1, below the Boltzmann value, and thus below a Boltzmann distribution of populations. This is demonstrated in figure 2.

The ratio increases linearly at first, following coronal equilibrium. However, at large n_e values, the population ratio approaches a Boltzmann distribution, as dictated by LTE conditions. For forbidden lines associated with low transition probabilities (A-values), LTE conditions - and thus a Boltzmann-like population distribution - are reached for lower electron densities. Although excitation rates are low, the atom or ion, once excited, has very little probability of decaying other than by spontaneous radiation Thorne et al. (2007).
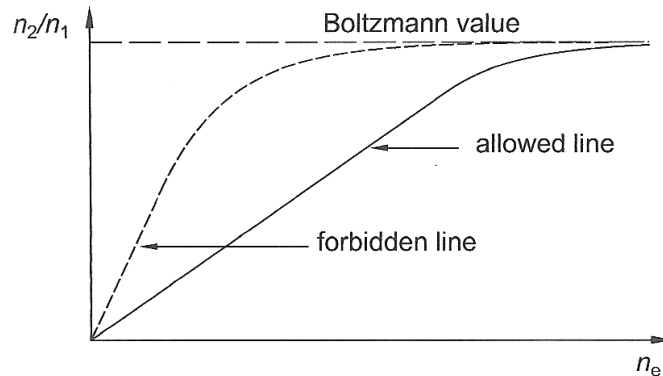
Figure 2: Population ratio n_2/n_1 for a two level atomic system plotted as a function of electron density n_e when the two levels are connected by an allowed transition (solid curve) or by a forbidden transition (broken curve), (Thorne et al., 2007).

According to Smith (2002), observations of IR spectra of Weigelt blobs, the Fan, the Little Homunculus and the polar lobes of the Homunculus indicate that gas near the equator is radiationally excited, whilst polar ejecta is dominated by collisional excitation. In connection to our framework, this suggests that the Sr-filament experiences an incident UV flux that dominates the radiation balance. However, even if levels are populated to reflect the incident UV flux, a relatively high electron density at $\sim 10^7$ cm^{-3} allow forbidden lines - and thus metastable states to approach a Boltzmann distribution at a higher rate than allowed transitions. It is assumed that the population of metastable states, to a first approximation, follow a Boltzmann distribution as

$$\frac{n_2}{n_1} = \frac{g_2}{g_1} \cdot e^{\Delta E/k_B T} \tag{6}$$

Under nebulae conditions that can be approximated with coronal equilibrium, the observed intensity of a spectral line is proportional to the spontaneous transition probability and the population of the metastable state, such that $I_{21} \propto n_2 A_{21}/\lambda_{21}$. In the low density regime, the line emission from each level is therefore, in extension, directly proportional to the population of the upper state, and thus to the collisional excitation of the two levels, expressed as a function of atomic parameters and temperature. Assuming two metastable states with different excitation potentials and radiating through parity forbidden transitions, the difference in excitation potentials makes the relative collisional excitation sensitive to temperature. Drawing upon the connection to the assumed Boltzmann distribution of metastable states, an expression for temperature diagnostics is explicitly obtained

$$ln(\frac{I_{21}\lambda_{21}}{g_2 A_{21}}) = -\frac{E_2}{k_B T} + \frac{g_1}{C} \tag{7}$$

Where ΔE has been rewritten as E_2 by restricting the transitions to those from a metastable upper state to the groundstate, and the factor g_1/C is a at a constant value corresponding to the y-intercept, associated with the experimental instrumentation. Plotting equation 7 as $log(I\lambda/gA)$ against E_2 for

parity-forbidden spectral lines generates a Boltzmann plot, with a theoretical straight line of slope $1/k_B T$, giving a measure of the temperature.

If two upper levels in a pair of forbidden lines have similar excitation energy, such as two fine-structure levels, the collisional excitation probability is temperature independent, and the couple can be used for electron density diagnostics. In the lower electron density regime, every collisional excitation is followed by radiative decay. The observed line intensity is therefore determined by the rate of excitation, which is determined by the statistical weight of the level. For two fine structure levels, the relative intensity is thus proportional to the ratio of the statistical weights, such that $I_1/I_2 = g_1/g_2$. For high electron densities, level populations conform to the LTE conditions of a Boltzmann distribution. In this regime, the number of states undergoing radiative decay prior to state quenching is proportional to the associated A-values, which differs for different states. This makes forbidden line-couples intensity ratio sensitive to collisional deexcitation which governs the equilibrium balance. The intensity ratio is therefore proportional to the product of the statistical weight and the associated A-values, such that $I_1/I_2 \propto g_1/g_2 \cdot A_1/A_2$. The intermediate electron density domain generates intensity ratios determined by the competition between the radiative and the collisional deexcitation of the excited levels. Equilibrium equations must be set up and solved, with A_i expressed in terms of known atomic parameters, Osterbrock & Ferland (2006).

3 Experiment and Analysis

3.1 Instrument and Observation

3.1.1 X-Shooter

Xshooter is a second generation instrument at VLT, constructed by consortium of Institutes in Denmark, France, Italy the Netherlands together with ESO. It is a multiwavelength ($\lambda\lambda 300 - 2500nm$) medium resolution spectrograph mounted on a UTH Cassegrain focus. Incident light is decomposed into the three spectral ranges, each one associated with an arm with optimised optics, dispersive elements and detectors for observations in $\lambda 300 - 559.5nm$, $\lambda 559.5 - 1024nm$ and $\lambda 1024 - 2480nm$ respectively. Each arm consists of a cross dispersed echelle spectograph, and the spectral format of each arm is fixed. Three piezo controlled mirrors located in front of each arm correct for differential atmospheric refraction between the guiding wavelength and the central wavelength. An internal calibration unit, equipped with pen-ray (Ar, He, Ne, and Xe), Th-Ar, Halogen and D2 lamps produces calibration frames, Vernet J., et al (2011).

By definition, NIR spectroscopy is not subject to atmospheric distortions and other seeing effects to the same extent as other wavelength regions. The NIR arm covers a range of 1020 - 2480 nm, engulfing 16 spectral orders.

According to table 2, the resolving power of the Xshooter NIR spectrograph assures distinguished line structures within the range $\Delta\lambda = 0.094 - 0.230 \ nm$, assuming a slitwidth of 0.4".

Table 2: X-Shooter NIR arm spectrograph resolving power Vernet (2011).

Slit Width (")	$R = \lambda/\Delta\lambda$
0.4	10500
0.6	7780
0.6JH	7760
0.9	5300
0.9JH	5300
1.2	3890

3.1.2 The Sr-filament Near-Infrared (NIR) Spectra

Long-slit spectra of η Car from $\lambda\lambda 990 - 2410 nm$ using the NIR arm of the ESO X-Shooter instrument at VLT were obtained to conduct the analysis. The Homunculus was sampled during the middle of the spectroscopic cycle on regular 0.5" interval long-slit aperture spectra positioned so as to align with the equatorial skirt in the plane perpendicular to the polar axis, with aperture centred on the central star. Two spectra at position offsets 2.0 and 3.0 arcsec to the NW were chosen for analysis. Wavelengths were calibrated by internal instrumentation at Xshooter location. The raw data is of .fits format, with information categorised into wavelength and flux. Telluric atmospheric absorption is observed in the spectra.

3.2 Analysis Procedure

3.2.1 Line Identification

The spectra are analysed using the Scientific Data Visualisation Software IDL (Interactive Data Language), package. From the IDL command window the spectra are superimposed on a common plot of flux as a function of wavelength. Since the spectra are obtained at different positions from the central object, and because of small scale variations in atmospheric seeing conditions between the times of data acquisition, the flux measurements in the spectra differ. A crude normalisation was performed by multiplying the flux measurement of the 3.0 arcsec spectra by a factor such that the large-scale continuum level was comparable. For visualization, see Figure 3.

The spectrum, offset from the Sr-filament, acts as a filter of the normalised spectra, and a comparison of the two spectra determines emission lines characteristic of the Sr-filament. The wavelength-position of the characteristic Sr-filament emission lines are accurately measured with the IDL *lineplot* script. Wavelength measurements are corrected for dopplershift following the expected characteristic 100 kms^{-1} velocity structure of the Sr-filament. Assuming the doppler formula $\Delta\lambda/\lambda = v/c$, a correction factor for the wavelength measurements can be formulated as

$$\lambda_0 = \lambda(1 - \frac{v_{srf}}{c}) = 1.000333675 \cdot \lambda \tag{8}$$

where λ_0 is the tabulated laboratory wavelength, λ is the raw Sr-filament wavelength, v_{srf} is the characteristic velocity of the Sr-filament and c is the speed of light. The correction factor was applied to the measurements.
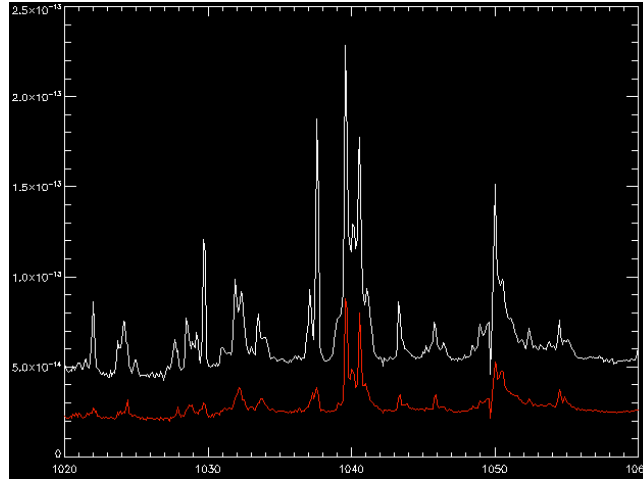
(a) The two spectra, superimposed on one plot prior to normalization.
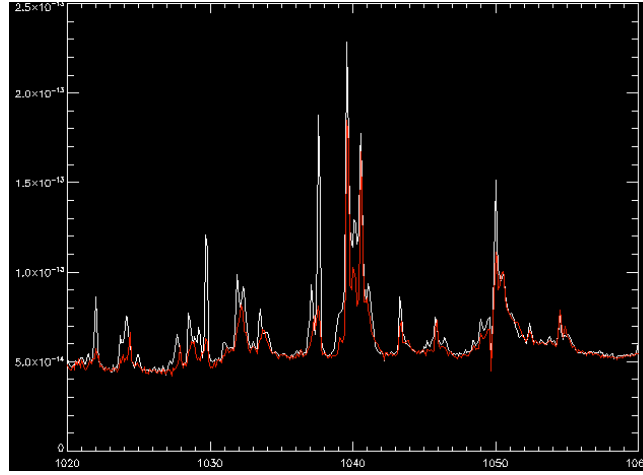
(b) The two spectra, superimposed on one plot after normalization.

Figure 3: The 2" offset spectrum centred on the Sr-filament is shown in white. The 3" offset "filter"-spectrum is shown in red. (a) Shows the spectra superimosed in the same plot prior to normalization. (b) Shows the two spectra superimposed in the same plot after normalization. Plot (b) enables comparison of line strengths, allowing the identification of lines intrinsic to the Sr-filament. Notice the difference in line-strength between the two spectra for the lines around $\lambda 1030 nm$ and $\lambda 1037.5 nm$.

To identify a transition and the associated ion, the doppler corrected measurements, λ_0's were compared with tabulated line-lists, (NIST Database), (Kurucz database), and Charlotte E. Moores' *Multiplet Table of Astrophysical Interest*, Moore (1945a). According to previous studies, emission lines of an ion in the Sr-filament on average follow a velocity spread of $\pm 6\ kms^{-1}$ corresponding to a wavelength spread of $\pm 0.04\ nm$, Hartman et al. (2004). Therefore, all tabulated atomic transitions within a range of $\pm 0.04\ nm$ of the corrected wavelength measurements are proposed as candidates. The candidate list for a given transition is reduced by identifying ions observed in previous studies. Assuming

a wavelength fit from a previously unknown element abundance, located within the spread of the measurement and conforming to further analytical constrains on possible candidates, the transition is tabulated as a candidate and possible blend.[1]

From the interplay between intrinsic atomic properties and population considerations, the candidate lists are narrowed down further. In general, the parameters that determine the intensity of a line reflect the underlying physical conditions. At the low density limit, excitations are rare, and consequently an upper-level population cannot be maintained. Therefore, every excitation will produce a deexcitation that is not subject to statistical selection based on the magnitude of the associated A-values of different decay channels. Thus, the intensity of the line becomes independent of the transition strength, and the A-value no longer acts as a selection mechanism of the decay channel. As the density increases, conditions result in a maintained upper state population. The atomic transition probability therefore dictates the likelihood of a transition through a specific decay channel - and thus of the strength of the associated transition. A larger A-value translates into higher intensity. Assuming two transitions from *different* ions make up the identified candidates, the transition (and thus the ion) with the largest A-value will contribute *more* to the weighted intensity. In principle, the ion transition with the lower A-value *cannot* be ruled out. However, depending on the difference between the magnitudes of the compared A-values, its contribution to the weighted intensity may be minimal, and for all intents and purposes, can be neglected for the ion transition of the larger A-value. Assuming two transitions from the *same* ion make up the identified candidates, the situation is further complicated. Under such conditions, the transitions tend to be confined to the same - or energetically similar upper and lower states, such as finestructure or hyperfine structure levels. Similar to the previous discussion, the assigned A-values determine the weighted intensity contribution from each transition, the difference being that there is an internal competition between the levels for the the electrons. Depending on the difference between the A-values, the larger A-value transition will empty/vacate the population of the upper state prior to any lower A-value transition occurring.

For the transition probability to become an effective tool in the process of line identification, the atomic state considered must be populated. At local thermodynamic equilibrium (LTE), atomic states are populated according to the Boltzmann distribution, with a population that falls as $n \propto Exp(\Delta E)$. At densities of $10^7\ cm^{-1}$, the Sr filament resides in a temperature dependent transition region, governed by the interplay between photoexcitation from an incident UV flux from the central source, equations of LTE conditions and equations of Corona Equilibrium conditions. From previous discussion (Section 2.3), it follows that the population of atomic states is described by equations governing the intermediate region between the extreme regimes. However, to a first approximation, one can assume that the population falls of with an increased ΔE, resulting in a lower registered intensity. By similar reasoning as for atomic probability, the weighted intensity of a transition with a large upper state population will exceed that of a transition with a low upper state population. Put differently; in the choice between transitions, the transition associated with the

---

[1]The underlying assumption throughout the analysis being that extensive previous studies have identified all ions characteristic of the Sr-filament. Thus, larger constrains are placed on new candidate ions.

energetically lowest upper state will dominate the registered intensity.

The transition probability and the population distribution have been defined under ideal conditions, in a general sense, without external influences or mechanisms acting.[2] The interplay between the two is applied on to each line to further reduce the possible candidates. The probability of a certain candidate is reinforced by identification of other lines originating from the same upper level (confirming the existence of a population).The resulting linelist with associated transition probability and upper state energy is tabulated in Section 4, Table 3.

3.2.2   Temperature Diagnostics

Identified [TiII] emission lines are abundant as compared with parity-forbidden lines of other ions, spanning a wavelength region of $\lambda\lambda \ 997 - 1189 \ nm$, and encompassing excitation potentials ranging $E_k = 1.08 - 1.24 \ eV$. A lack of atomic reference data prevents any temperature diagnostics from being conducted. The suggested emission lines are tabulated as a candidate dataset for future temperature diagnostics by means of forbidden transitions and Boltzmann plots.

4   Results

4.1   Line Identification

Table 3: Spectral emission lines identified in the Sr-filament of η Car in the wavelength region $\lambda\lambda$ 9950-24100 nm. Spectral lines are categorised according to wavelength, with transitions defined in terms of spectroscopic notation. Atomic parameters of line-identification and line-diagnostic relevance are tabulated. λ_{obs} defines spectral lines corrected for a doppler shift corresponding to a characteristic velocity $v_{sr-filament} = 100 kms^{-1}$. Forbidden lines denoted by "[ ]" refer to M1 and E2 forbidden transitions. Lines with more than one plausible candidate are listed with the same measured wavelength, λ_{obs}. Atomic parameters and rest wavelengths are identified with Kramide, A., and Ralchenko, Yu., and Read, J., and NIST ASD Team (2012), Smith, P., and Heise, C., and Esmond, J., and Kurucz, R. (2012), Moore (1945b) and Moore (1945a).

$\lambda_{obs_{air}}$	$\lambda_{lab_{air}}$	Ion	Multiplet Transition	E_k	A_{ik}
(nm)	(nm)			(eV)	(s^{-1})
997.63	997.2590	[TiII]	a $^4F_{3/2}$ - b $^4P_{5/2}$	1.240	
999.93	999.8310	[FeI]	a $^5F_3$ - a $^5P_2$	2.198	$3.900 \cdot 10^{-3}$
1000.74	1000.7280	FeI	b $^3G_3$ - y $^5F_3$	4.256	$1.449 \cdot 10^2$
1006.65	1006.6950	[TiII]	a $^4F_{3/2}$ - b $^4P_{3/2}$	1.231	$7.500 \cdot 10^{-3}$
1006.65	1006.7040	[TiII]	a $^4F_{5/2}$ - b $^4P_{5/2}$	1.243	$3.000 \cdot 10^{-3}$
1012.59	1012.5960	[TiII]	a $^4F_{3/2}$ - b $^4P_{1/2}$	1.224	$3.5 \cdot 10^{-2}$
1016.31	1016.3595	FeII	z $^4D_{7/2}$ - b $^4G_{7/2}$	6.730	$1.066 \cdot 10^3$
1016.31	1016.3130	[TiII]	a $^4F_{5/2}$ - b $^4P_{3/2}$	1.230	
1018.33	1018.3522	CaI	3d4p $^3D_2$ - 4s10d $^3D_3$	5.956	$6.252 \cdot 10^4$

Continued on next page

---

[2]Note that the whilst the interplay between the atomic transition probability and the population distribution defines the selection criterion of the line list, it is discussed independently of the transition. For a forbidden transition, the selection criteria remains the same, but the interplay is different because of the prolonged lifetime of the metastable state.

$\lambda_{obs_{air}}$	$\lambda_{lab_{air}}$	Ion	Multiplet Transition	E_k	A_{ik}
(nm)	(nm)			(eV)	(s^{-1})
1018.33	1018.2863	NaI	4p $^2P_{3/2}$ - 9d $^2D_{3/2}$	4.971	$5.322 \cdot 10^4$
1018.33	1018.2863	NaI	4p $^2P_{3/2}$ - 9d $^2D_{5/2}$	4.971	$3.236 \cdot 10^5$
1018.75	1018.8100	[CoII]	$3d^8$ $^3F_4$ - $4s$ $^3F_4$	1.210	
1020.20	1020.2050	[TiII]	a $^4F_{7/2}$ - b $^4P_{5/2}$	1.240	
1022.33	1022.3270	[TiII]	a $^4F_{5/2}$ - b $^4P_{1/2}$	1.220	
1022.33	1022.3270	[CrII]	a $^4G_{9/2}$ - a $^4H_{11/2}$	3.740	
1024.51	1024.5400	[CoII]	$3d^8$ $^3F_3$ - $4s$ $^3F_3$	1.320	
1030.09	1030.0860	[TiII]	a $^4F_{7/2}$ - b $^4P_{3/2}$	1.230	
1032.24	1032.2608	ScII	3d5s $^3D_2$ - 3d5p $^3P_0$	8.336	$2.782 \cdot 10^7$
1034.14	1034.1893	VII	c $^3D_1$ - w $^3D_2$	6.679	$2.610 \cdot 10^3$
1037.98	1037.9730	[TiII]	a $^4F_{9/2}$ - b $^4P_{5/2}$	1.240	
1039.96	1039.9330	[ScII]	a$^1D_2$ - a$^3P_2$	1.500	
1040.93	1040.9194	CaI	4s16d $^1D_2$ - 3d5f $^3D_1$	7.245	$1.306 \cdot 10^5$
1041.48	1041.4734	CaI	4s7d $^3D_2$ - 3d4f $^3D_1$	6.931	$1.302 \cdot 10^5$
1046.16	1046.1950	[ZrII]^3	a $^2P_{5/2}$ - d $^2D_{3/2}$	2.170	
1050.35	1050.3470	[TiII]	a $^4F_{3/2}$ - a $^4P_{5/2}$	1.180	
1060.36	1060.3650	[ZrII]	a $^4F_{5/2}$ - b $^4P_{3/2}$	1.200	
1064.01	1064.0190	[TiII]	a $^4F_{3/2}$ - a $^4P_{3/2}$	1.160	
1067.64	1067.6610	[TiII]	a $^4F_{3/2}$ - a $^4P_{1/2}$	1.160	
1074.28	1074.2557	FeI	b $^3D_3$ - y $^3D_2$	4.795	$1.636 \cdot 10^3$
1074.28	1074.2803	FeI	(^{3}F)sp $^5D_1$ - (^{4}F)4d f $^3D_2$	6.703	$5.844 \cdot 10^4$
1074.75	1074.7120	NaI	4p $^2P_{3/2}$ - 9s $^2S_{1/2}$	4.907	$2.189 \cdot 10^5$
1074.75	1074.7640	[TiII]	a $^4F_{5/2}$ - a $^4P_{3/2}$	1.160	
1075.29	1075.3002	FeI	(^{5}D)sp z $^3D_1$ - d^8 $^3P_0$	5.112	$7.225 \cdot 10^5$
1075.82	1075.8320	[TiII]	a $^4F_{7/2}$ - a $^4P_{5/2}$	1.180	
1075.82	1075.8040	[CrII]	a $^4P_{3/2}$ - a $^4F_{5/2}$	3.840	
1078.48	1078.5428	VII	c $^1D_2$ - w $^3D_3$	6.686	$3.794 \cdot 10^3$
1078.48	1078.4916	CaI	3d4p $^3P_2$ - 4s15s $^3S_1$	6.027	$8.773 \cdot 10^2$
1078.48	1078.4800	[TiII]	a $^4F_{5/2}$ - a $^4P_{1/2}$	1.160	
1083.45	1083.4907	NaI	3d $^2D_{3/2}$ - 6f $^2F_{5/2}$	4.761	$2.119 \cdot 10^6$
1083.45	1083.4846	NaI	$2p^63d$ $^2D_{5/2}$ - $2p^66f$ $^2F_{7/2}$	4.761	$2.245 \cdot 10^6$
1083.45	1083.4846	NaI	$2p^63d$ $^2D_{5/2}$ - $2p^66f$ $^2F_{5/2}$	4.761	$1.500 \cdot 10^5$
1094.06	1094.0371	FeI	(^{3}F)sp $^5D_4$ - (^{4}F)4d f $^5P_3$	6.591	$4.214 \cdot 10^4$
1095.61	1095.6984	ScII	3d5p $^3P_0$ - 4p^2 b $^3P_1$	9.468	$1.372 \cdot 10^6$
1095.61	1095.6100	[TiII]	a $^4F_{9/2}$ - a $^4P_{7/2}$	1.180	
1107.97	1108.002	[TiII]	b $^4F_{3/2}$ - b $^4P_{3/2}$	1.230	
1111.95	1111.9797	FeI	b $^3P_1$ - z $^3D_1$	3.960	$1.018 \cdot 10^5$
1111.95	1111.9800	FeI	b $^3P_1$ - z $^3D_1^o$	3.940	
1112.82	1112.7833	FeI	b $^3H_4$ - z $^5G_3$	4.415	$4.275 \cdot 10^2$
1115.05	1114.9471	VII	c $^3F_2$ - z $^3G_3$	4.864	$5.073 \cdot 10^4$
1125.07	1125.1116	FeI	b $^3P_0$ - z $^3D_1$	3.960	$1.665 \cdot 10^5$
1125.07	1125.1090	FeI	b $^3P_0$ - z $^3D_1^o$	3.940	
1138.15	1138.1454	NaI	3p $^2P_{1/2}$ - 4s $^2S_{1/2}$	3.191	$8.520 \cdot 10^6$

<div align="right">Continued on next page</div>

---

^{3}A recent term analysis of ZrII indicates that the transition is wrongly identified. Analysis shows that the d $^2D_{3/2}$ state is assocaited with an excitation potential of 3.427 eV, Nilsson (2013).

$\lambda_{obs_{air}}$	$\lambda_{lab_{air}}$	Ion	Multiplet Transition	E_k	A_{ik}
(nm)	(nm)			(eV)	(s^{-1})
1138.15	1138.1210	NaI	$3\,^2P^o_{1/2}$ - $4\,^2S_{1/2}$	3.180	
1140.38	1140.3779	NaI	3p $^2P_{3/2}$ - 4s $^2S_{1/2}$	3.191	$1.693 \cdot 10^7$
1140.38	1140.3550	NaI	$3\,^2P^o_{3/2}$ - $4\,^2S_{1/2}$	3.180	
1160.29	1160.2939	FeI	x $^5P_3$ - e $^5S_2$	6.342	$1.853 \cdot 10^4$
1160.29	1160.2410	[TiII]	a $^4F_{5/2}$ - a $^2D_{3/2}$	1.080	
1160.69	1160.7570	FeI	a $^5P_2$ - z $^5D^o_2$	3.250	
1171.54	1171.5498	FeI	s ^{6}D)5s e $^5D_1$ - (^{4}F)5p $^5D_2$	6.700	$1.424 \cdot 10^5$
1171.54	1171.5502	CaI	4s4d $^3D_2$ - 4s8p $^3P_1$	5.739	$1.228 \cdot 10^6$
1171.54	1171.4280	[TiII]	b $^4F_{5/2}$ - a $^4P_{5/2}$	1.180	
1173.54	1173.5520	[TiII]	a $^4F_{7/2}$ - a $^2D_{5/2}$	1.080	
1183.89	1183.8997	CaII	5s $^2S_{1/2}$ - 5p $^2P_{3/2}$	7.515	$2.372 \cdot 10^7$
1183.89	1183.8549	VII	c $^3D_2$ - x $^3D_1$	6.522	$1.924 \cdot 10^4$
1183.89	1183.8665	FeI	y $^3G_5$ - e $^3G_5$	6.663	$1.175 \cdot 10^3$
1183.89	1183.9201	FeI	y $^5G_6$ - e $^7G_5$	6.352	$5.283 \cdot 10^3$
1185.80	1185.7960	[TiII]	b $^4F_{7/2}$ - a $^4P_{5/2}$	1.180	
1188.46	1188.4082	FeI	a $^5P_1$ - z $^5D_2$	3.266	$7.621 \cdot 10^4$
1188.46	1188.4570	[TiII]	b $^4F_{5/2}$ - a $^4P_{3/2}$	1.160	
1189.64	1189.6250	FeI	y $^3G_3$ - h $^5D_2$	6.691	$2.692 \cdot 10^3$
1189.64	1189.6480	[ScII]	a $^1D_2$ - b $^1D_2$	1.350	
1193.39	1193.3600	[TiI]	a $^5F_5$ - a $^3G_5$	1.880	
1194.39	1194.3750	[CrII]	a $^6D_{5/2}$ - a $^4G_{7/2}$	2.530	
1197.23	1197.3041	FeI	a $^5P_3$ - z $^5D_4$	3.200	
1203.57	1203.5861	FeI	(^{2}F)4s d $^3F_3$ - (^{3}P)sp $^3D_2$	5.614	$8.222 \cdot 10^3$
1215.96	1215.9212	FeI	e $^5D_4$ - y $^3I_5$	6.559	$3.317 \cdot 10^2$
1229.75	1229.7153	FeI	x $^5D_4$ - e $^5F_3$	5.921	$1.615 \cdot 10^4$
1242.10	1242.1021	CaI	3d4p $^3P_0$ - 4s10s $^3S_1$	5.875	$2.030 \cdot 10^5$
1244.82	1244.8255	CaI	3d4p $^1F_3$ - 4s13d $^3D_2$	6.022	$1.502 \cdot 10^4$
1244.48	1244.8784	FeI	w $^5D_2$ - g $^5D_1$	6.474	$7.542 \cdot 10^4$
1256.89	1256.6800	[FeII]	a $^6D_{9/2}$ - a $^4D_{7/2}$	9.834	$2.730 \cdot 10^6$
1263.82	1263.8700	FeI	y $^5P_3$ - e $^5D_4$	5.539	$6.416 \cdot 10^5$
1297.98	1297.9681	CaI	4p^2 $^1D_2$ - 4s13p $^1P_1$	6.004	$5.666 \cdot 10^5$
1298.75	1298.7746	CrII	(^{5}D)4d e $^6P_{3/2}$ - (^{5}D)5p $^4F_{5/2}$	11.670	$1.495 \cdot 10^4$
1319.92	1319.8965	TiII	c $^2D_{5/2}$ - z $^4D_{7/2}$	4.063	$7.290 \cdot 10^2$
1327.44	1327.4244	FeI	z $^5I_5$ - e $^5G_6$	6.264	$1.336 \cdot 10^3$
1327.74	1327.7770	[FeII]	a $^6D_{3/2}$ - a $^4D_{5/2}$	1.040	$1.170 \cdot 10^{-3}$
1442.10	1442.0858	FeI	(^{3}P)sp $^3D_2$ - s ^{4}D)5s g $^5D_1$	6.474	$3.089 \cdot 10^3$
1443.98	1443.9882	FeI	(^{4}F)5s e $^5F_4$ - (^{3}D)sp $^5D_4$	6.733	$4.411 \cdot 10^4$
1449.18	1449.1734	VII	c $^3F_3$ - z $^3D_3$	4.613	$2.828 \cdot 10^2$
1449.47	1449.4528	ScII	3d4d $^1P_1$ - 3d5p $^3P_1$	8.344	$2.215 \cdot 10^4$
1468.91	1468.8752	FeI	(^{3}F)sp $^5D_1$ - s ^{6}D)4d e $^7G_1$	6.393	$1.678 \cdot 10^3$
1488.89	1488.8793	CaI	4s6d $^3D_3$ - 3d5p $^3D_3$	6.418	$9.618 \cdot 10^5$
1490.53	1490.5253	FeI	y $^5S_2$ - e $^5G_3$	6.350	$2.173 \cdot 10^4$
1490.88	1490.8870	MgI	s5p $^3P_2$ - 13d $^1D_2$	7.558	$1.067 \cdot 10^4$
1496.24	1496.2988	FeI	(^{3}F)sp $^5D_4$ - s ^{6}D)4d e $^5G_5$	6.286	$5.721 \cdot 10^3$
1497.08	1497.1122	FeI	w $^5D_2$ - e $^7P_2$	6.306	$1.369 \cdot 10^4$
1497.49	1497.4349	FeI	(^{3}F)sp $^3F_3$ - (^{4}F)4d f $^5G_4$	6.667	$2.910 \cdot 10^4$

$\lambda_{obs_{air}}$ (nm)	$\lambda_{lab_{air}}$ (nm)	Ion	Multiplet Transition	E_k (eV)	A_{ik} (s^{-1})
1507.70	1507.7289	FeI	e $^5D_3$ - u $^5P_3$	6.409	$1.307 \cdot 10^6$
1513.16	1513.1643	FeI	e $^5D_3$ - u $^3G_4$	6.406	$4.908 \cdot 10^5$
1514.11	1514.1411	FeI	(^{3}F)sp $^5F_1$ - s ^{6}D)4d f ^5D	6.321	$1.155 \cdot 10^5$
1519.15	1519.1124	FeI	(^{4}F)5s e $^5F_5$ - (^{4}F)5p $^5G_5$	6.644	$6.114 \cdot 10^3$
1519.51	1519.5218	VII	c $^3D_2$ - y $^3P_1$	6.291	$1.356 \cdot 10^4$
1526.71	1526.7051	FeI	d^8 $^3P_2$ - (^{3}P)sp $^1D_2$	5.879	$5.005 \cdot 10^4$
1526.71	1526.7084	FeI	w $^5G_2$ - e $^3G_3$	6.742	$3.208 \cdot 10^3$
1534.53	1534.4992	FeI	w $^5D_2$ - f $^5D_2$	6.286	$4.325 \cdot 10^4$
1537.48	1537.5412	CaI	3d4p $^1F_3$ - 4s8d $^3D_2$	5.832	$7.857 \cdot 10^3$
1541.58	1541.6428	FeI	(^{3}F)sp $^5D_2$ - s ^{6}D)4d e $^5S_{1/2}$	6.342	$5.623 \cdot 10^3$
1544.18	1544.1833	FeI	(^{4}F)5s e $^5F_4$ - (^{4}F)5p $^5G_3$	6.677	$1.414 \cdot 10^5$
1546.41	1546.4820	CaI	4p^2 $^1D_2$ - 4s9p $^1P_1$	5.850	$2.229 \cdot 10^5$
1555.93	1555.9849	FeI	x $^3G_4$ - e $^5H_4$	6.725	$4.392 \cdot 10^2$
1600.61	1600.5784	CaI	4s6p $^3P_0$ - 4s15d $^3D_1$	6.046	$6.070 \cdot 10^4$
1612.95	1613.1774	FeI	(^{3}F)sp $^5D_2$ - s ^{6}D)4d e $^7P_2$	6.306	$1.240 \cdot 10^4$
1616.34	1616.3699	MgI	s5p $^3P_1$ - 10d $^1D_2$	7.493	$4.873 \cdot 10^4$
1626.23	1626.2877	FeI	(^{3}F)sp $^5F_3$ - s ^{6}D)4d f $^5D_2$	6.286	$1.029 \cdot 10^3$
1634.25	1634.2002	VII	c $^1D_2$ - y $^3D_2$	6.295	$2.675 \cdot 10^3$
1656.40	1656.3869	FeI	v $^5F_1$ - g $^5F_1$	6.743	$3.338 \cdot 10^4$
1664.05	1664.0668	FeI	e $^5F_3$ - x $^3F_3$	6.666	$4.390 \cdot 10^5$
1678.06	1678.0392	CaI	4s6p $^3P_2$ - 4s14s $^3S_1$	6.011	$5.665 \cdot 10^3$
1679.89	1679.8305	FeI	s ^{6}D)5s e $^5D_4$ - s ^{6}D)5p $^7P_3$	6.277	$5.191 \cdot 10^3$
1717.32	1717.3892	FeI	(^{4}F)5s e $^5F_1$ - (^{4}F)5p $^5D_2$	6.700	$3.063 \cdot 10^6$
1727.77	1727.7530	CaI	4s5d $^3D_2$ - 4s12f $^3F_2$	6.017	$8.810 \cdot 10^3$
1727.77	1727.7560	FeI	s ^{6}D)4d e $^7G_6$ - SEJ s^4 f $^7G_7$	7.037	$1.694 \cdot 10^5$
1741.74	1741.7383	CaI	4s4f $^1F_3$ - 4s10d $^1D_2$	5.962	$8.769 \cdot 10^5$
1741.74	1741.7028	VII	e $^3P_1$ - x $^3P_2$	6.784	$4.571 \cdot 10^2$
1742.59	1742.6306	FeI	x $^5G_4$ - e $^7S_3$	6.394	$5.412 \cdot 10^2$
1799.49	1799.5071	CaI	4s16p $^3P_1$ - 3d4d $^3P_2$	6.733	$7.973 \cdot 10^2$
1799.49	1799.5071	CaI	4s16p $^3P_2$ - 3d4d $^3P_2$	6.733	$2.017 \cdot 10^2$
1808.42	1808.4070	FeI	v $^3G_3$ - f $^3F_2$	6.866	$4.845 \cdot 10^3$
1808.42	1808.4489	FeI	(^{4}F)5s e $^5F_1$ - (^{4}F)5p $^5F_2$	6.664	$2.149 \cdot 10^4$
1809.84	1809.8862	FeI	w $^5P_2^o$ - e $^5P_3$	6.427	$2.325 \cdot 10^4$
1895.57	1895.5200	MgI	3s4f $^3F_3^o$ - 3s8g $^3G_4$	7.433	$4.140 \cdot 10^5$
1895.57	1895.5300	MgI	3s4f $^3F_4^o$ - 3s8g $^3G_5$	7.433	$4.42 \cdot 10^5$
1895.57	1895.5400	MgI	3s4f $^3F_4^o$ - 3s8g $^3G_4$	7.433	$2.76 \cdot 10^4$
1940.39	1940.3585	FeI	(^{3}F)sp $^1F_3$ - (^{4}F)4d e $^3G_3$	6.742	$5.433 \cdot 10^2$
1940.74	1940.6991	FeI	(^{4}P)4p $^3D_2$ - s ^{4}D)5s e $^3D_1$	6.452	$2.499 \cdot 10^3$
1958.70	1958.6388	FeI	z $^3S_1$ - f $^5F_2$	6.411	$9.354 \cdot 10^3$
1991.76	1991.7195	CaI	4s4p $^3P_2$ - 3d4s $^3D_1$	2.521	$9.779 \cdot 10^3$
2057.93	2057.9231	FeI	(^{4}F)5p $^5G_3$ - s ^{4}D)4d g $^5G_3$	7.279	$1.109 \cdot 10^3$
2059.79	2059.8150	VII	e ^3P - w $^3D_1$	6.664	$1.107 \cdot 10^2$
2079.90	2079.9162	FeI	z $^3F_2$ - d $^3F_2$	4.580	$3.183 \cdot 10^3$
2089.17	2089.2345	FeI	x $^5G_3$ - f $^5D_2$	6.286	$2.500 \cdot 10^2$
2090.46	2090.4935	FeI	(^{4}F)5p $^5D_2$ - s ^{4}D)4d g $^5G_2$	7.293	$1.369 \cdot 10^4$
2112.42	2112.4429	FeI	y $^5G_4$ - e $^5F_3$	5.921	$4.889 \cdot 10^4$

Continued on next page

$\lambda_{obs_{air}}$	$\lambda_{lab_{air}}$	Ion	Multiplet Transition	E_k	A_{ik}
(nm)	(nm)			(eV)	(s^{-1})
2112.42	2112.3817	FeI	(^{4}F)5s e $^3F_2$ - (^{3}D)sp $^5F_3$	6.653	$2.038 \cdot 10^2$
2159.82	2159.8816	FeI	(^{3}D)sp $^5D_3$ - s ^{4}D)4d g $^5G_4$	7.256	$9.501 \cdot 10^3$
2205.65	2205.6426	NaI	4s $^2S_{1/2}$ - 4p $^2P_{3/2}$	3.753	$6.680 \cdot 10^6$

4.2 Temperature Diagnostics

Table 4: Forbidden [TiII] lines of astrophysical importance in temperature and density parameter diagnostics. Intensity measurements are obtained by integrating over the line profile. For accurate intensity measurements, a Voight profile should be fitted to account for Lorenzian wings. However, constrains in the fitting procedure limited profile adaptations to Gaussian fits. A.U. denotes "arbitrary units".

$\lambda_{lab_{air}}$	I_{ik}	Notes
(nm)	A.U.	
997.2590	$4.26 \cdot 10^{-15}$	
1006.695	$1.41 \cdot 10^{-13}$	
1006.704	$3.37 \cdot 10^{-15}$	
1012.596	$3.37 \cdot 10^{-15}$	
1016.313	$1.02 \cdot 10^{-14}$	
1020.205	$7.52 \cdot 10^{-15}$	
1022.327	$6.62 \cdot 10^{-15}$	
1030.086	$1.42 \cdot 10^{-14}$	
1037.973	$2.39 \cdot 10^{-14}$	
1050.347	$1.67 \cdot 10^{-14}$	Large Error in Fit
1064.019	$2.81 \cdot 10^{-15}$	
1067.661	$7.81 \cdot 10^{-15}$	
1074.764	$8.25 \cdot 10^{-15}$	
1075.832	$7.72 \cdot 10^{-15}$	
1078.480	$4.23 \cdot 10^{-15}$	
1095.610	$1.99 \cdot 10^{-14}$	
1108.002	$1.09 \cdot 10^{-15}$	
1160.241	-	No Gaussian Fit
1171.428	$5.74 \cdot 10^{-15}$	
1173.552	$1.18 \cdot 10^{-14}$	
1185.796	$5.87 \cdot 10^{-15}$	
1188.457	$5.29 \cdot 10^{-14}$	

5   Discussion

Table 3 displays the identified emission lines in the wavelength region $\lambda\lambda 990 - 2410\ nm$. The results indicate that the NIR spectral region of the Sr-filament is dominated by intrinsic CaI, TiII and FeI emission lines, that account for $\backsim 75\%$ of the identified lines (Table 5). CaI and FeI lines tend to be spread throughout the observed spectral range, whilst TiII lines are located towards the lower spectral region, with transitions from the lowest terms roughly grouped into multiplets. The line distribution in the observed wavelength range reflects the complex atomic structure of iron that gives rise to transitions throughout the electromagnetic spectrum. Furthermore, the *abundance* of lines from the ions that dominate the spectrum acts as a self-consistent confirmation that those are the correctly identified lines from a range of candidates. Similarly, the proposed identification of lines from ions such as CaII remains borderline; whilst its ionic presence is supported by previous studies Hartman et al. (2004), the identified transition cannot be verified within the scope of this analysis nor by other multiplet lines.

  Four ions with transitions corresponding to Zr II (two lines) and Co II (two lines) not identified by Hartman et al. (2004) are tabulated. However, a recent term analysis of ZrII reveals that the parity-forbidden transition $a^2P_{5/2}$ - $d^2D_{3/2}$ at a rest-wavelength $\lambda 1046.1950$, as reported by Moore (1945a) and Moore (1945b) is wrongly identified, Nilsson (2013). Analysis reveals that the d $^2D_{3/2}$ state is associated with an excitation potential of 3.427 eV, Nilsson (2013).

  The large number of [TiII] lines, suggested by the percentage comparison in Table 5, and by Table 4 for parameter diagnostics, may be a result reflecting a large-scale problem, emanating from literature rather than an objective observation of the spectral region itself. In accordance with observations performed by Hartman et al. (2004), TiII is abundant. However, due to lack of atomic reference data towards the longer wavelength region of the spectrum, lines - and in particular forbidden transitions - may be underrepresented, leading to faulty conclusions regarding the optimal ions used for temperature and density diagnostics. As is observed in Table 5, the number of SrII and CaI lines present in the spectra point to a disagreement in the results of the conducted studies. However, analysis of associated energy levels indicate that the disagreement arises as a consequence of the atomic properties of the ions. Whilst the ions have theoretical transitions that fall within the spectral ranges of both studies, the upper levels associated with those transitions are located at different excitation potentials in the term diagrams of the ions. The physical conditions therefore dictate which states are populated, and thus explains the disagreement in the number of observed ion transitions. To generalise the argument, it may not be so strange that the relative percentages in the different spectral regions of the different studies differ. The atomic structure, and the electron configuration dictates in which spectral region and how many transitions in that region an ion will radiate. Thus, systematic variations between ion percentages may reflect the nature of the atomic system rather than an inherent disagreement between different studies.

  It should be noted that the limit excitation potential for ions has been increased compared to the study conducted by Hartman et al. (2004). This has primarily been done to account for potential borderline candidates, rather than

Table 5: Comparison of identified emission lines in spectral region $\lambda\lambda 990 - 2410\ nm$ with Hartman et al. (2004) tabulated lines in spectral region $\lambda\lambda 248 - 1014\ nm$. Note that the debated ZrII has been included for the sake of completeness.

Ion	Line-Count	Percentage %	Line-Count$_{Hartman}$	Percentage$_{Hartman}$ %
CI	-	-	3	0.53
Na I	11	7.64	2	0.36
Mg I	5	3.47	1	0.18
Al II	-	-	1	0.18
Ca I	18	12.50	1	0.18
Ca II	1	0.69	7	1.26
Sc II	5	3.47	43	7.73
Ti II	24	16.67	188	33.81
V II	9	6.25	101	18.17
Cr II	4	2.78	37	6.65
Mn II	-	-	31	5.58
Fe I	63	43.75	104	18.71
Fe II	2	1.39	17	3.06
Co II	2	1.39	8	1.44
Ni II	-	-	8	1.44
Sr II	-	-	4	0.72
Zr II	2	1.39	-	-

the risk of excluding transitions. This, in itself, is an assumption that is reflected in the results. Whilst a lower upper energy may only have yielded one or two potential candidates for a transition, an increased excitation potential opens up for a transition overlap from various ions at different population distributions, and thus contributes to form blended features in the line-list.

A line-list of unidentified transitions is found in the Appendix, Table 6. The 3 arcsec spectrum, used as a filter, suggests that these lines are associated to intrinsic emission of the Sr-filament. However, the ions and the associated electronic states responsible for the transitions have not been identified. The lines may indicate the presence of ions not previously associated with the Sr-filament. Alternatively, it must be recognised that using the 3 arcsec spectrum as a filter may have worked well for strong lines and large abundances, but may not account for the presence of other ions. The lines may be associated with various other structures in the line of sight, moving at other characteristic velocities such as the equatorial skirt, the receding northwest polar lobe of the Homunculus and the Little Homunculus. In this case, a doppler-shift correction corresponding to a velocity of $-100\ kms^{-1}$ may have resulted in wavelengths that are not characteristic of any atoms or ions. Lastly, the resolution of the XShooter instrumentation, and doppler-broadened features may contribute to form complex blends that resemble broad features from an original rich narrow-line spectrum with a weighted intensity maximum at a wavelength not belonging to any known atomic transition up to date.
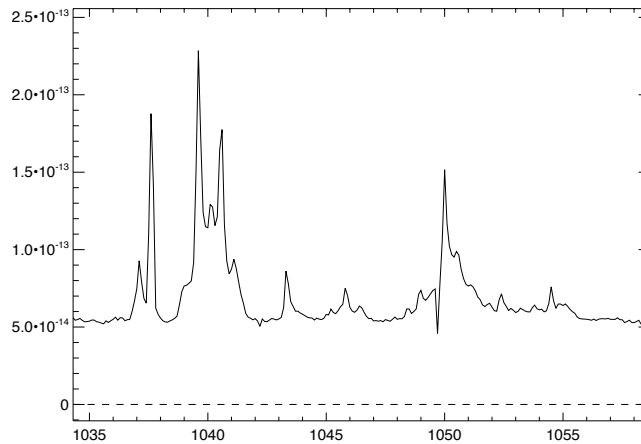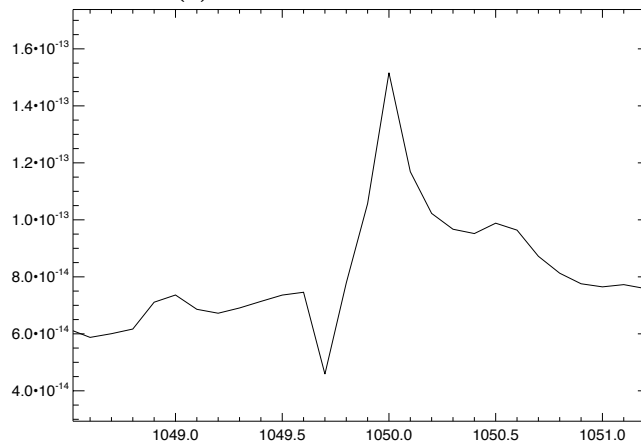
(a) Local Peak Environment

(b) [TiII] $\lambda 1050.347$ Emission Structure

Figure 4: A lineprofile of the $\lambda = 1050.347$ nm [TiII] line exemplifying the problem of Gaussian fittings in the obtained data. The profile is a blend, with an absorption feature close to the continuum level towards lower wavelength, and an emission line blend towards higher wavelength. Alternatively, the asymmetry in the line profile is caused by an unresolved flag-structure, formed as a result of the resolution and sampling of the instrument.

The number of [TiII] lines observed is comparably large, spanning a wavelength region of $\lambda\lambda 997 - 1189$ nm and an excitation potential of $1.08 - 1.24$ eV, thus making it a potential candidate for temperature diagnostics. Temperature diagnostics by means of Boltzmann plots is sensitive to a number of factors. The integration over the line profile must extend far enough to include the far wings, assuming the line profile has a significant Lorentzian component. Furthermore, the baseline has to be carefully chosen to exclude scattered light and the underlying continuum, and the method is insensitive unless the excitation potential covers a reasonably wide energy range, usually implying a wide wavelength region, making the calibration of the spectrometer difficult, Thorne et al. (2007). It should be noted that the values for the line-profile integrated

intensities in this thesis results is one of the main sources of errors for future diagnostics. Apart from the lack of reference atomic data, causing the lines not to be subjected to the test of the Boltzmann plot (which, apart from giving a value on the temperature parameter also acts as a test, to see if the candidates conform to the theoretical framework), the Gaussian fit was uncertain due to the problem of encompassing Lorenzian wings - a consequence due to the resolution and sampling of the spectrum, and due to the presence of telluric absorption profiles from the atmosphere in the spectra. The problem is conveyed in Figure 4.

6   Conclusion

The results indicate that the NIR spectral region of the Sr-filament is dominated by intrinsic CaI, TiII and FeI emission lines, accounting for $\smile$ 75% of the identified emission features. Though previous studies have indicated large abundances of these ions, other spectral regions such as the UV region, explored by Hartman et al. (2004) have also identified extensive amounts of emission lines belonging to VII. Such VII transition abundances are not present in the NIR spectra. One Zr II lines and two Co II lines not identified by Hartman et al. (2004) are identified. However, the results need to be confirmed by further studies.

Identified lines are grouped differently depending on the ion concerned, the clearest contrast being that of FeI spanning the entire spectral range whilst TiII tends to be located towards the lower spectral region, grouped in multiplets. The large span associated with FeI transitions reflects the variation in the possible electronic configurations that give rise to complex spectra. A bias in the atomic reference data on the atomic structure of TiII is present. However, where atomic reference data exists, the grouping of TiII lines is evident. Whilst the number of [TiII] lines is comparably large, spanning a wavelength region of $\lambda\lambda 997 - 1185$ nm and an excitation potential of $1.08 - 1.243\ eV$, thus making it a potential candidate for temperature diagnostics, lack of atomic reference data - specifically transition probabilities - limits any further analysis on the matter.

The analysis performed, and the results obtained, are based upon the second spectrum (3"), spatially separated from the Sr-filament, that acts as a filtering mechanism. The resulting line-list of the Sr-filament reflects lineprofiles that are significantly different wavelength-wise and intensity-wise from the 3" spectrum. It is therefore possible, that weak lines characteristic of the Sr-filament have been judged too-alike those of the 3" spectrum, or that they have been mistaken for noise. Future endeavours on the spectrum should include other "filtering techniques", or other selection criteria as a whole. Optimally, the spectrum should be investigated *without* a filter, comparing relative dopplershifts of pairs of lines. Additionally, the spectrum contains numerous lines from other spatial regions in the nebulae and inner ejecta surrounding Eta Carinae, which are of great interest but beyond the scope of this thesis.

References

Bautista, M. A., Gull, T. R., Ishibashi, K., Hartman, H., & Davidson, K. 2002, Monthly Notices of the RAS (MNRAS), 331, 875

Davidson, K. 1999, in Eta Carinae at the Millennium

Hamann, F. 2012 (Springer New York Dordrecht Heidelberg London: Springer Science + Business Media, LCC 2012), ISBN 978 - 1 - 4614 - 2274 - 7

Hartman, H., Gull, T., Johansson, S., Smith, N., & HST Eta Carinae Treasury Project Team. 2004, Astronomy and Astrophysics (A&A), 419, 215

Kramide, A., and Ralchenko, Yu., and Read, J., and NIST ASD Team. 2012, NIST National Institute of Standards and Technology, Internet, http://physics.nist.gov/cgi-bin/ASD/lines1.pl

Moore, C. 1945a, A MULTIPLET TABLE OF ASTROPHYSICAL INTEREST, revised edition edn. No. 20 (Princeton, New Jersey: Princeton University Observatory), PART I - TABLE OF MULTIPLETS

—. 1945b, A MULTIPLET TABLE OF ASTROPHYSICAL INTEREST, revised edition edn. No. 20 (Princeton, New Jersey: Princeton University Observatory), PART II - FINDING LIST

Nilsson, H. 2013, private Communication

Osterbrock, D., & Ferland, G. 2006, Astrophysics of Gaseous Nebulae and Active Galactic Nuclei, second edition edn. (Sausalito, California, United States of America: University Science Books)

Smith, N. 2002, Monthly Notices of the RAS (MNRAS), 337, 1252

Smith, N., Morse, J. A., Collins, N. R., & Gull, T. R. 2004, The Astrophysical Journal (ApJ), Letters, 610, L105

Smith, P., and Heise, C., and Esmond, J., and Kurucz, R. . 2012, Atomic Spectral Database from CD-ROM 23 R.L. Kurucz, Internet, http://www.cfa.harvard.edu/amp/ampdata/kurucz23/sekur.html

Thorne, A., Litzen, U., & Johansson, S. 2007, Spectrophysics Principles and Applications (Lund, Sweden: Media-Tryck Lund)

Vernet, J. e. a. 2011, X-shooter, the new wide band intermediate resolution spectrograph at the ESO Very Large Telescope, European Space Observatory ESO, Internet, /xshooter/doc/xshooter_Vernet2011

7   Appendix

Table 6: Unidentified lines. λ_{raw} defines the raw data measurements prior to the applied doppler correction of the Sr-filament. λ_{obs} defines doppler corrected measurements assuming a characteristic Sr-filament velocity of 100 kms^{-1}. The raw measurements are given to account for the potential errornous assumption of the lines being intrinsic to the Sr filament.

$\lambda_{raw_{air}}$	$\lambda_{obs_{air}}$
(nm)	(nm)
996.300	997.630
1002.68	1003.01
1003.20	1003.53
1004.80	1005.14
1027.67	1028.01
1037.63	1037.98
1043.33	1043.68
1048.99	1049.34
1060.67	1061.02
1068.20	1068.56
1067.98	1068.34
1068.78	1069.14
1070.99	1071.35
1082.71	1083.07
1117.90	1118.27
1118.37	1118.74
1124.36	1124.74
1140.00	1140.38
1159.71	1160.10
1160.30	1160.69
1181.30	1181.69
1182.02	1182.41
1182.94	1183.33
1185.40	1185.80
1188.52	1188.92
1192.62	1193.02
1194.54	1194.94
1202.20	1202.60
1202.82	1203.22
1203.17	1203.57
1217.11	1217.52
1238.20	1238.61
1241.11	1241.52
1243.73	1244.15
1247.04	1247.46
1249.18	1249.60
1257.20	1257.62
1264.65	1265.07

Continued on next page

$\lambda_{raw_{air}}$	$\lambda_{obs_{air}}$
(nm)	(nm)
1268.71	1269.13
1281.63	1282.06
1293.34	1293.77
1294.77	1295.20
1296.77	1297.20
1297.55	1297.98
1305.09	1305.53
1316.98	1317.42
1327.61	1328.05
1357.71	1358.16
1362.94	1363.39
1415.58	1416.05
1447.47	1447.95
1455.48	1455.97
1455.69	1456.18
1464.06	1464.55
1474.05	1474.54
1482.05	1482.54
1474.70	1475.19
1478.20	1478.69
1480.79	1481.28
1482.40	1482.89
1484.60	1485.10
1488.19	1488.69
1488.84	1489.34
1490.73	1491.23
1493.27	1493.77
1499.90	1500.40
1507.60	1508.10
1508.01	1508.51
1512.26	1512.76
1519.00	1519.51
1525.86	1526.37
1526.58	1527.09
1534.54	1535.05
1544.10	1544.62
1543.66	1544.18
1544.30	1544.82
1546.45	1546.97
1552.80	1553.32
1555.80	1556.32
1569.84	1570.36
1587.85	1588.38
1600.08	1600.61
1610.79	1611.33
1611.32	1611.86

Continued on next page

$\lambda_{raw_{air}}$	$\lambda_{obs_{air}}$
(nm)	(nm)
1611.78	1612.32
1615.80	1616.34
1623.74	1624.28
1624.29	1624.83
1627.86	1628.40
1633.82	1634.37
1640.50	1641.05
1642.25	1642.80
1644.10	1644.65
1656.45	1657.00
1664.37	1664.93
1668.10	1668.66
1677.50	1678.06
1678.50	1679.06
1680.49	1681.05
1687.09	1687.65
1687.90	1688.46
1700.06	1700.63
1709.82	1710.39
1710.85	1711.42
1711.80	1712.37
1716.75	1717.32
1717.10	1717.67
1727.81	1728.39
1733.61	1734.19
1734.95	1735.53
1735.99	1736.57
1798.60	1799.20
1808.28	1808.88
1808.90	1809.50
1809.24	1809.84
1865.61	1866.23
1936.60	1937.25
1937.08	1937.73
1938.08	1938.73
1950.67	1951.32
1951.40	1952.05
1954.30	1954.95
1956.97	1957.62
1974.36	1975.02
2045.70	2046.38
2056.56	2057.25
2057.82	2058.51
2058.46	2059.15
2077.59	2078.28
2080.48	2081.17

Continued on next page

$\lambda_{raw_{air}}$	$\lambda_{obs_{air}}$
(nm)	(nm)
2116.80	2117.51
2119.48	2120.19
2133.45	2134.16
2136.60	2137.31
2142.91	2143.63
2144.88	2145.60
2158.05	2158.77
2165.25	2165.97
2203.88	2204.62
2207.70	2208.44
2217.75	2218.49
2218.70	2219.44
2239.86	2240.61
2241.59	2242.34
2243.26	2244.01
2242.52	2243.27
2347.76	2348.54
2348.21	2348.99
2348.80	2349.58
2405.19	2405.99